Chapter 5

Scattering by a flux tube

5.1 Introduction§

A problem of considerable interest and more recently, controversy, relates to the influence of magnetic fields on acoustic waves in the near surface regions of the Sun. In these sub-photospheric magnetic regions, the ratio of magnetic to gas pressure is very close to unity, leading to the contention that magnetic field effects are systematic and significant. However, due to the difficulties involved in modeling magnetic field effects, most helioseismic analyses tend to ignore these effects, lumping them all into a 'surface term'. The scientific merit of results that invoke this assumption have come into question and in particular, inversions of sunspots have attracted much debate. Owing to the intense magnetic field strengths and the inclination of the field in the penumbra (e.g. Schunker et al., 2003), sunspot structure and dynamics inversions (e.g. Duvall et al., 1996; Couvidat, Birch, & Kosovichev, 2006) have been a source of considerable discussion. Some of these inversions (Couvidat, Birch, & Kosovichev, 2006) use finite-wavelength descriptions of the acoustic wavefield derived from the approximated constituent equations in the Born limit (Birch, Kosovichev & Duvall, 2004). Gizon, Hanasoge, & Birch (2006) showed that although the first

§ *The results of this chapter are reproduced from Hanasoge, Birch, Bogdan, & Gizon (2007). I wrote this paper, produced all the graphs and did all the calculations. This is work in progress and some sections will be added before submitting it to a journal.*

Born approximation may be valid in regions where the magnetic to gas pressure ratio is much less than unity, its applicability in regions of high magnetic to gas pressure ratios such as sunspots is highly debatable.

Mode conversion (e.g. Barnes & Cally, 2000) is a phenomenon commonly associated with magnetic field induced scattering. From one acoustic mode to another, from acoustic modes to Alfvèn waves and so on, it is estimated that acoustic energy is somewhat redistributed and otherwise lost (in the conversion to Alfvèn waves), contributing perhaps to p-mode absorption observed in sunspots (Braun, 1995). The mode absorption in sunspots detected by Braun (1995) is substantial and until the causal factors are conclusively determined, the relatively simplistic pure acoustic approach in the handling of active regions and sunspots is further threatened.

Kernels are functions that relate perturbations to the consequent travel-time anomalies. Birch, Kosovichev & Duvall (2004) introduced kernels that account for finite wavelength effects to invert for interior sound-speed perturbations. However, obtaining finite-wavelength kernels that invert for magnetic fields has long been a problem of interest for the reason that they allow us to recover the interior magnetic structure. Mathematically speaking, it is a difficult proposition to construct such a kernel from the wave equations because of the complex nature of the Lorentz force term and the induction equation. Applying techniques of time-distance helioseismology (Duvall et al., 1993) on f modes, Duvall, Gizon & Birch (2006), have a extracted kernel for thin magnetic elements from careful measurements of thousands of isolated, small magnetic features. This kernel contains the experimental scattering properties of an 'average' flux tube, information that can be used to establish the effectiveness of theoretical models.

In an attempt to construct an analytical framework to decipher the nature of wave interaction with magnetic regions, Bogdan & Cally (1995), Bogdan et al. (1996) and Barnes & Cally (2000) model a magnetic flux concentration in the thin tube limit placed in a truncated polytrope. Essentially, the flux tube is assumed to be thin enough that variations across its interior are neglected; moreover the tube must be a sub-wavelength feature and the radius small in comparison to the pressure scale height. The parameters of the polytrope are selected so as to mimic the solar sub-photospheric layers as closely as possible and is truncated a little below the photosphere because the rapidly diminishing density makes the thin tube approximation inapplicable very close to the surface.

Bogdan et al. (1996) have demonstrated that the dominant flux tube mode is the kink mode and that the f mode couples strongly with the flux tube. Moreover, measurements of Duvall, Gizon & Birch (2006) are for f modes. Consequently, the focus of this chapter will be to quantify the interaction between an incoming f mode and the resulting kink mode exhibited by the flux tube. Over the next few sections, we describe the analytical model in greater detail, followed by a discussion of the numerical method we apply to extract the scattering coefficients. We then compute the traveltime shifts associated with the flux tube using the method described in Gizon, Hanasoge, & Birch (2006) and compare the phase and amplitudes of the scattered waves with those obtained by Duvall, Gizon & Birch (2006). We conclude with a summary of our calculations and a discussion of the relevance and importance of these results.

5.2 The model

The background model is chosen to be an adiabatically stratified, truncated polytrope with index $m = 1.5$, gravity $\mathbf{g} = -2.775 \times 10^4$ cm s$^{-2}\mathbf{e_z}$, reference pressure $p_0 = 1.21 \times 10^5$ g cm^{-1} s^{-2} and reference density $\rho_0 = 2.78 \times 10^{-7}$ g cm^{-3}, such that the pressure and density variations are given by,

$$p(z) = p_0 \left(-\frac{z}{z_0}\right)^{m+1}, \tag{5.1}$$

and

$$\rho(z) = \rho_0 \left(-\frac{z}{z_0}\right)^{m}. \tag{5.2}$$

We utilize a right-handed cylindrical co-ordinate system in our calculations, with co-ordinates $\mathbf{x} = (r, \theta, z)$ and corresponding unit vectors $(\mathbf{e_r}, \mathbf{e_\theta}, \mathbf{e_z})$. The photospheric level of the background model is at $z = 0$, with the upper boundary placed at a depth of $z_0 = 392$ km. Applying the model of Barnes & Cally (2000), a lower boundary is placed at a depth of 98 Mm. The displacement potential $\Psi(\mathbf{x}, t)$ describing the oscillation modes (t is time) is required to enforce zero Lagrangian pressure perturbation boundary conditions at both boundaries, and is given by:

$$\Psi(\mathbf{x}, t) = \sum_{m=-\infty}^{\infty} i^m N_n s^{-1/2-\mu} J_m(k_n r) e^{i[m\theta - \omega t]} \left[\zeta_n^p M_{\kappa_n^p,\mu}\left(\frac{s\nu^2}{\kappa_n^p}\right) + M_{\kappa_n^p,-\mu}\left(\frac{s\nu^2}{\kappa_n^p}\right)\right]. \tag{5.3}$$

In equation 5.3, we introduce a slew of new symbols,

$$\mu = \frac{m-1}{2}, \quad \nu^2 = \frac{m\omega^2 z_0}{g}, \quad k_n^p = \frac{\nu^2}{2\kappa_n^p z_0}, \tag{5.4}$$

ω the circular frequency of oscillation, $s = -z/z_0$, $J_m(w)$, the Bessel function of order m and argument w and $M_{\kappa,\mu}(w)$, the Whittaker function (e.g. Whittaker & Watson, 1980) with indices κ, μ and argument w. The eigenvalue $\kappa_n^p > 0$ and constant ζ_n^p characterizing the mode are obtained through the procedure described in appendix E. The $n = 0$ mode corresponds to the surface gravity or f mode, while $n > 0$ represents the acoustic p_n mode. The term N_n is the normalization constant for the mode, defined as

$$N_n = \left[\int_1^{\infty} \left[\zeta_n^p M_{\kappa_n^p,\mu}\left(\frac{\nu^2 s}{\kappa_n^p}\right) + M_{\kappa_n^p,-\mu}\left(\frac{\nu^2 s}{\kappa_n^p}\right)\right]^2 ds\right]^{-1/2}. \tag{5.5}$$

5.2.1 Flux tube

Applying the approximations listed in cf. 2 of Bogdan et al. (1996), a thin flux tube carrying a magnetic flux of $\Phi_f = 3.88 \times 10^{17}$Mx, with plasma-$\beta = 1$ everywhere inside the tube is placed in the polytrope. The thin flux tube approximation,

$$b(s) \approx \sqrt{\frac{8\pi p(s)}{1+\beta}}, \qquad \pi R^2(s) \approx \frac{\Phi_f}{b(s)}, \tag{5.6}$$

where $b(s)$ and $R(s)$ are the magnetic field and the radius of the tube at depth s, is shown to be accurate to better than a percent in the truncated polytrope situated below $z = -z_0$ or $s = 1$ (Bogdan et al., 1996).

5.2.2 Oscillations of the tube: the kink mode

Motions of the flux tube created by the impinging modes (whose displacement potential is given by $\Psi(\mathbf{x}, t)$) are described by $\xi(s, t)$, a solution to the differential equation

$$\left[z_0 \frac{\partial^2}{\partial t^2} + \frac{2gs}{(1+2\beta)(m+1)} \frac{\partial^2}{\partial s^2} - \frac{g}{1+2\beta} \frac{\partial}{\partial s} \right] \xi = \frac{2(1+\beta)}{1+2\beta} z_0 \frac{\partial^3 \Psi}{\partial x \partial t^2}, \tag{5.7}$$

where $x = r\cos\theta$. Following Bogdan et al. (1996), we define $\xi_\perp = -i\tilde{\xi}(s)$, where $\xi(s,t) = \tilde{\xi}(s)e^{-i\omega t}$, and $\tilde{\xi}(s)$ is the purely spatial component of the tube displacement. The function $\xi_\perp$ contains all of the scattering information that is needed to understand the interaction of the wavefield with the flux tube.

5.2.3 Jacket modes and a lower boundary

Bogdan & Cally (1995) showed that scattered waves created as a consequence of magnetic interactions are a mixture of modal and evanescent components. The scattering process results in not only a redistribution (and loss) of modal energies but also in the production of a continuous spectrum of evanescent 'modes' called *jacket modes*. Mathematically, this uncountable infinity of jacket modes arises as a consequence of the lower boundary being placed at $s = \infty$. A description of jacket modes requires extensive use of Whittaker functions, which are relatively difficult and expensive to compute accurately. Moreover, the jacket mode equations listed in Bogdan & Cally (1995) contain integrals over running indices that pose significant numerical hurdles because of the poor convergence properties of the integral. In order to circumvent any calculations involving these continuous jacket modes, we employ a lower boundary placed at a depth $s = D = 250$ to reduce this uncountably infinite set of evanescent modes to a more manageable discrete countably infinite counterpart in the manner described in Barnes & Cally (2000).

Only modes whose inner turning points are in the vicinity of the lower boundary are affected by its presence and therefore, placing it at a depth of 98 Mm means that the f- and first few p modes remain untouched. Moreover, we expect the scattering amplitude to decay sharply with increasing radial order. Consequently, the high order p modes which interact with the lower boundary are largely unimportant in any case because of their weak contribution to the scattering process studied here. With the introduction of the boundary, the problem becomes numerically well defined as well.

In order to obtain the p- and jacket mode eigenfunctions, we apply a zero Lagrangian pressure perturbation lower boundary condition for the sake of simplicity (see the appendix in Barnes & Cally, 2000). We also assume that the tube oscillations ($\xi_\perp$ in Eq. [5.7]) are oblivious to the lower boundary. This condition is necessary because energy loss in the form of propagating Alfvèn waves along the tube can only occur when the lower boundary is transparent (not the case with zero Lagrangian pressure perturbation).

To summarize, we use the formalism and model of Bogdan et al. (1996) but unable to carry out calculations of the necessary jacket modes described in Bogdan & Cally (1995), we replace this uncommonly difficult continuous set of modes by its more tractable discrete cousin (Barnes & Cally, 2000). Next, we describe the tube radius boundary condition that allows us to begin the task of estimating the scattering coefficients.

5.2.4 The tube boundary

Since we are mainly interested in the interaction of the f mode with the flux tube, the velocity potential of the incident wave, denoted by $\Psi_{\rm inc}$ is given by:

$$\Psi_{\rm inc} = \sum_{m=-\infty}^{\infty} i^m J_m(k_0^p r)\Phi_p(\kappa_0^p; s)e^{i[m\theta-\omega t]}. \tag{5.8}$$

The resonant wavenumber of the p_n mode is denoted by k_n^p (including the $n = 0$ f mode), while wavenumbers corresponding to jacket modes are labelled k_n^J. The eigenvalues $\kappa_n^J > 0$ and κ_n^p are related to k_n^J and k_n^p respectively, according to equation (5.4) (replace p by J in Eq. 5.4). In equation 5.8,

$$\Phi_p(\kappa_n^p; s) = s^{-1/2-\mu}\left[\zeta_n^p M_{\kappa_n^p,\mu}\left(\frac{s\nu^2}{\kappa_n^p}\right) + M_{\kappa_n^p,-\mu}\left(\frac{s\nu^2}{\kappa_n^p}\right)\right]. \tag{5.9}$$

The scattered wave is given by (e.g. Bogdan & Cally, 1995)

$$\Psi_{\rm sc} = -\sum_{n=0}^{\infty}\sum_{m=-\infty}^{\infty} i^m \left[\alpha_{mn}^p H_m^{(1)}(k_n^p r)\Phi_p(\kappa_n^p; s) + \beta_{mn}^J K_m(k_n^J r)\Phi_J(\kappa_n^J; s)\right] e^{i[m\theta-\omega t]}, \tag{5.10}$$

where α_{mn}^p are the p-mode scattering coefficients, β_{mn}^J are the jacket mode coefficients and $K_m(w)$ is the K-Bessel function of order m and argument w. The un-normalized jacket mode eigenfunction, $\Phi_J(\kappa_n^J; s)$, is given by

$$\Phi_J(\kappa_n^J; s) = s^{-1/2-\mu}\left[\eta_n^J M_{-i\kappa_n^J,\mu}\left(\frac{i\nu^2}{\kappa_n^J}s\right) + M_{-i\kappa_n^J,-\mu}\left(\frac{i\nu^2}{\kappa_n^J}s\right)\right], \tag{5.11}$$

where η_n^J, a parameter and κ_n^J, the jacket mode eigenvalue are determined by the boundary conditions (see appendix A for details) and $M_{\kappa,\mu}(w)$ is the Whittaker function (Whittaker & Watson, 1980). The normal to the tube boundary at a given depth s is given by

$$\hat{\mathbf{n}} = \frac{\mathbf{e_r} - \frac{1}{z_0}\frac{dR}{ds}\mathbf{e_z}}{\left[1 + \left(\frac{1}{z_0}\frac{dR}{ds}\right)^2\right]^{1/2}}. \tag{5.12}$$

The boundary condition is then obtained by matching radial velocities across the tube boundary, $r = R(s)$,

$$\hat{\mathbf{n}}\cdot\boldsymbol{\nabla}\left[\Psi_{\rm inc} + \Psi_{\rm sc}\right]_{r=R(s)} = \hat{\mathbf{x}}\cdot\hat{\mathbf{r}}\xi_\perp(s)e^{-i\omega t}, \tag{5.13}$$

where $\hat{\mathbf{x}}$ is the unit vector along the x-axis. Simplifying equation (5.13), we obtain

$$\left[\frac{\partial}{\partial r}(\Psi_{\rm inc} + \Psi_{\rm sc}) - \frac{1}{z_0^2}\frac{dR}{ds}\frac{\partial}{\partial s}(\Psi_{\rm inc} + \Psi_{\rm sc})\right]_{r=R(s)} = e^{-i\omega t}\xi_\perp(s)\cos\theta\left[1 + \left(\frac{1}{z_0}\frac{dR}{ds}\right)^2\right]^{1/2}. \tag{5.14}$$

Using a least squares approach, equation (5.14) is then solved to obtain an estimate for the scattering coefficients α^p_{mn} and subsequently, the kernel.

5.3 Solution procedure

By only retaining the $|m| = 1$ coefficients and cancelling the $e^{-i\omega t}$ term in equation (5.14), time and angular dependencies may be eliminated. Because we are only dealing with a single m, the scattering coefficients introduced in equation (5.10) are rewritten as α^p_n, β^J_n. We define the following functions

$$f(s) = \frac{i\xi_\perp(s)}{2}\sqrt{1+\left(\frac{1}{z_0}\frac{dR}{ds}\right)^2} + \left(\frac{\partial}{\partial r} - \frac{1}{z_0^2}\frac{dR}{ds}\frac{\partial}{\partial s}\right)\left[J_1(k^p_0 r)\Phi_p(\kappa^p_0; s)\right]|_{r=R(s)}, \quad (5.15)$$

$$g^p_n(s) = \left(\frac{\partial}{\partial r} - \frac{1}{z_0^2}\frac{dR}{ds}\frac{\partial}{\partial s}\right)\left[H^{(1)}_1(k^p_n r)\Phi_p(\kappa^p_n; s)\right]|_{r=R(s)}, \quad (5.16)$$

$$g^J_n(s) = \left(\frac{\partial}{\partial r} - \frac{1}{z_0^2}\frac{dR}{ds}\frac{\partial}{\partial s}\right)\left[K_1(k^J_n r)\Phi_J(\kappa^J_n; s)\right]|_{r=R(s)}, \quad (5.17)$$

and arrive at the least-squares problem:

$$A\begin{pmatrix}[\alpha]\\ [\beta]\end{pmatrix} = \begin{pmatrix} f(s_1) \\ \dots \\ f(s_M)\end{pmatrix}. \quad (5.18)$$

In equation (5.18), s_1 and s_M (M is the number of grid-points in depth) are the start and end of the finite vertical domain, $[\alpha], [\beta]$ are column vectors of the scattering coefficients, α^p_n and β^J_n and the $M \times (N_1 + N_2 + 1)$ matrix A is given by:

$$A = \begin{pmatrix} g^p_0(s_1) & \dots & g^p_{N_1}(s_1) & g^J_1(s_1) & \dots & g^J_{N_2}(s_1) \\ \dots & \dots & \dots & \dots & \dots & \dots \\ g^p_0(s_M) & \dots & g^p_{N_1}(s_M) & g^J_1(s_M) & \dots & g^J_{N_2}(s_M) \end{pmatrix}, \quad (5.19)$$

where $N_1 + 1, N_2$ are the number of p- and jacket modes included in this calculation, respectively. The grid spacing in the s space was set at $\Delta s = 0.249$ or correspondingly,

Table 5.1. Scattering coefficients

Mode	Amplitude	Phase
f	0.00757	39.6
p_1	0.00042	74.7
p_2	0.00021	33.0
p_3	0.00020	12.6
p_4	0.00016	7.40
p_5	0.00011	5.93
p_6	0.00012	2.96

$\Delta z = 97$ km. For physical parameters, we utilize the model described in Bogdan et al. (1996), wherein $m = 1.5$, $\Phi = 3.88 \times 10^{17}$ Mx, $R(s = 1) = 100$ km, $z_0 = 392$ km, and incident modes of frequency, $\omega = 2\pi\nu, \nu = 2, 3, 4, 5$ mHz, and $\beta = 0.1, 1, 10$. The lower boundary of the box is set at $D = 250$ or 98 Mm. The thin flux tube approximation may be invoked to ignore the dependence of various terms on derivatives with respect to s in this calculation. Although not shown here, we verified the validity of this approximation by demonstrating the invariance of the scattering coefficients by calculating and comparing them with and without the derivative terms. The coefficients for the first 4 modes were seen to be stable to changes in the depth of the lower boundary, as discussed in §5.2.3.

A large number of jacket modes (463, 675, 820, 900 for $\nu = 2, 3, 4, 5$ mHz respectively) is required to fit the right hand side with the accuracy of Figure 5.1. The least squares fitting was performed using the backslash command in MATLAB. The various complementary and standard Whittaker functions were computed using CERNLIB, a freely available suite of mathematical functions. The absolute values of a sample of the scattering coefficients, $|\alpha_n^p|$ and corresponding phases, $\arg(\alpha_n^p)$ for plasma-$\beta = 1$ and $\nu = 3$ mHz are listed in the second and third columns of table 5.1. We do not display the jacket mode coefficients here.

Our confidence in these values is strengthened by the consistency of these scattering coefficients over a large number of numerical experiments. We show in the upper panels of figure 5.1 that the combination of resonant and jacket modes captures the right hand side very well. In the lower panels, the contributions of the jacket and resonant modes are separated to illustrate that jacket modes are a non-trivial component of the scattering process. Shown in figure 5.2 is the agreement with intuitive expectation that the higher the radial order of the p mode, the lower the contribution. This is in line with the idea that the scattering matrix (Braun, 1995) is nearly diagonal with weak off-diagonal terms that decay very rapidly. In Figure 5.4, we show the phases as a function of frequency, mode number and plasma-β associated the scattering.

5.4 Comparison

There is a definite dependence of the magnitude of the scattering coefficients on the plasma-β and the frequency of the incident wave. It emerges from our calculations that the wave - flux tube coupling becomes stronger as the frequency increases (see Figure 5.2 and 5.3). Moreover, as the flux tube becomes magnetically dominated ($\beta = 0.1$), the scattering is enhanced, as emphasized by the magnitudes of the scattering coefficients. Correspondingly, the flux tube becomes relatively stiff and the tube kink mode is more resistant to the buffeting forces of the interacting modes (upper panel of Figure 5.5). The reverse effect is observed for $\beta = 10$, where the tube is hydrodynamically dominated (lowest panel of Figure 5.5).

5.5 Discussion

We have presented a model of acoustic scattering off a magnetic flux concentration. Earlier efforts to model magneto-acoustic interactions (e.g. Gizon, Hanasoge, & Birch, 2006) have been under less realistic conditions because of the related mathematical difficulties. However, it is noted that this model is not as complex as in the solar case where phenomena such as radiative heat transfer, azimuthal asymmetries in the tube, the lack of applicability of the thin tube approximation, local changes in source properties, downflows, etc. probably play an important role in affecting the wavefield.

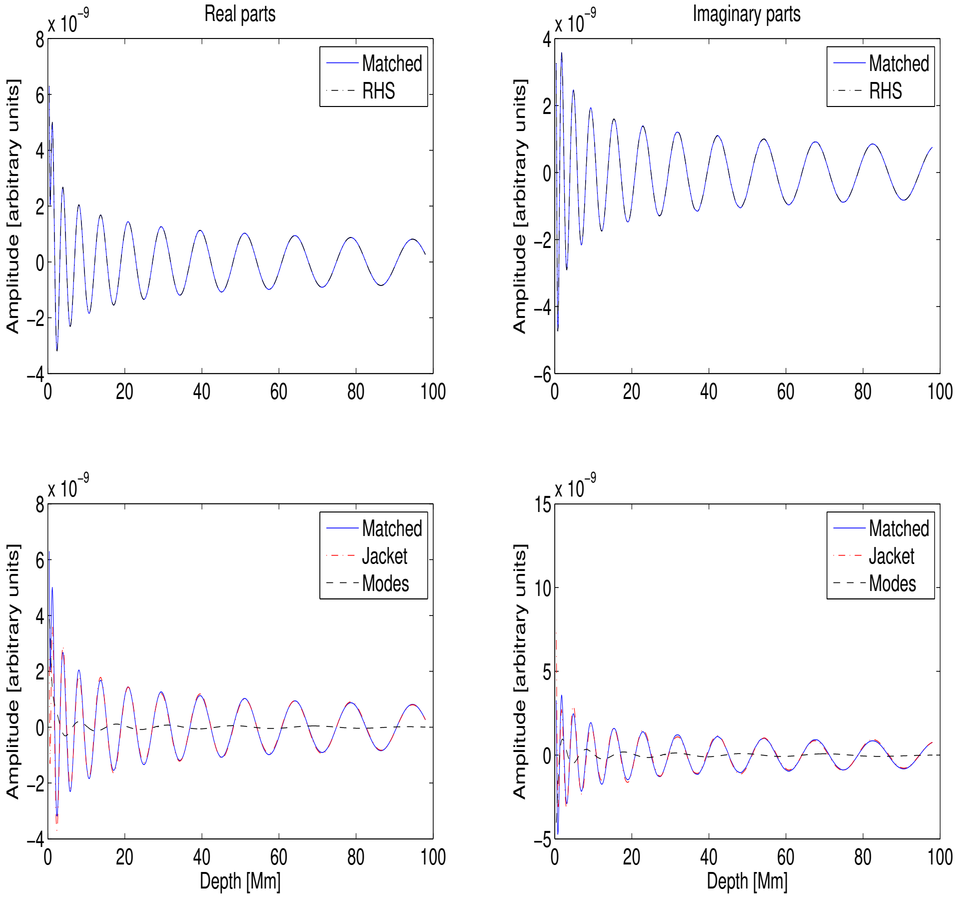

Figure 5.1 The upper panels show comparisons of real and imaginary parts of the fit (labeled 'matched' in the figure) to the corresponding real and imaginary parts of the right hand side (RHS) for $\beta = 1$ and $\nu = 5$ mHz. Contributions to the real and imaginary parts of the right hand side (RHS) respectively from the jacket and resonant modes are shown in the lower panels. The lower boundary was placed at a depth of 98 Mm; the surface gravity mode with 13 acoustic and 857 jacket modes were used in this matching.

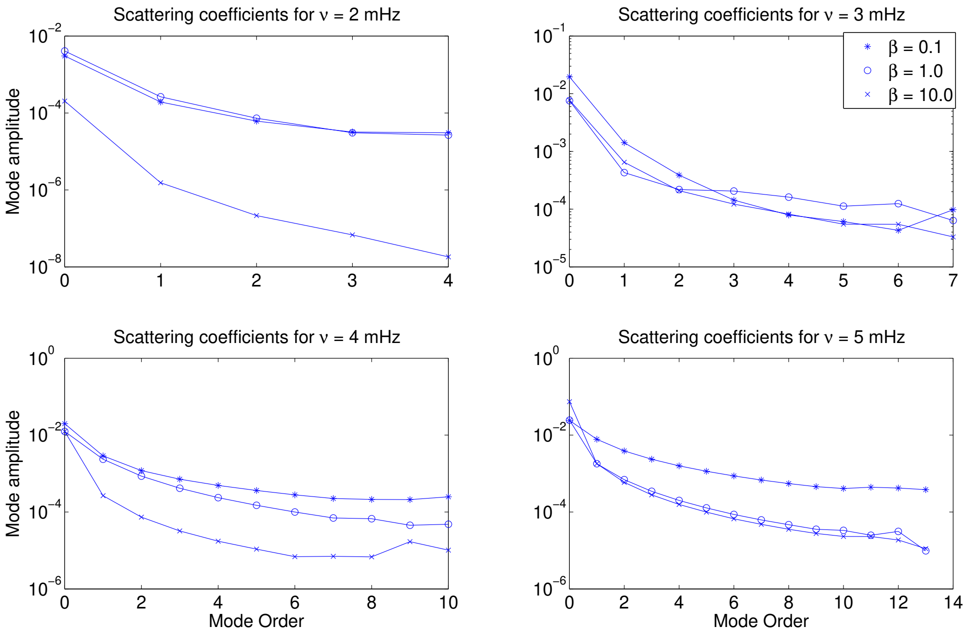

Figure 5.2 The amplitudes of the scattered resonant modes as a function of mode number shown for various values of plasma-β and frequency, ν. The legend applies to all panels.

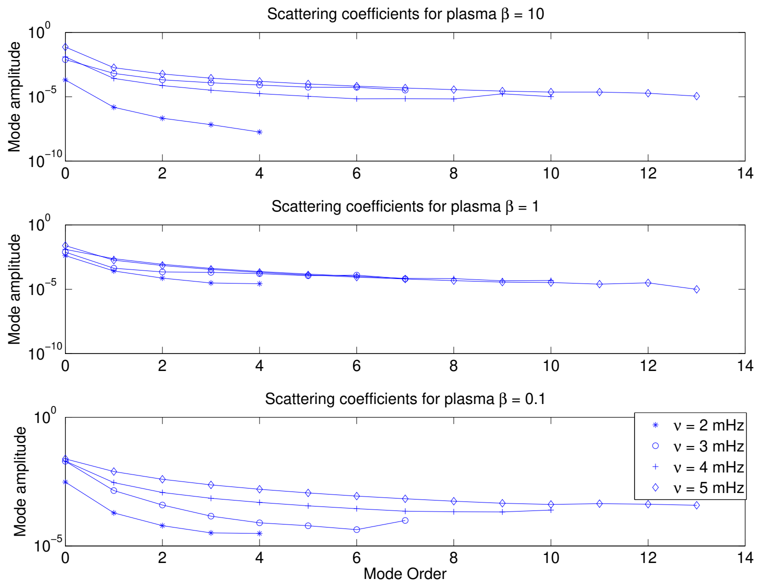

Figure 5.3 The amplitudes of the scattered resonant modes as a function of mode number shown for various values of plasma-β and frequency, ν. The legend applies to all panels.

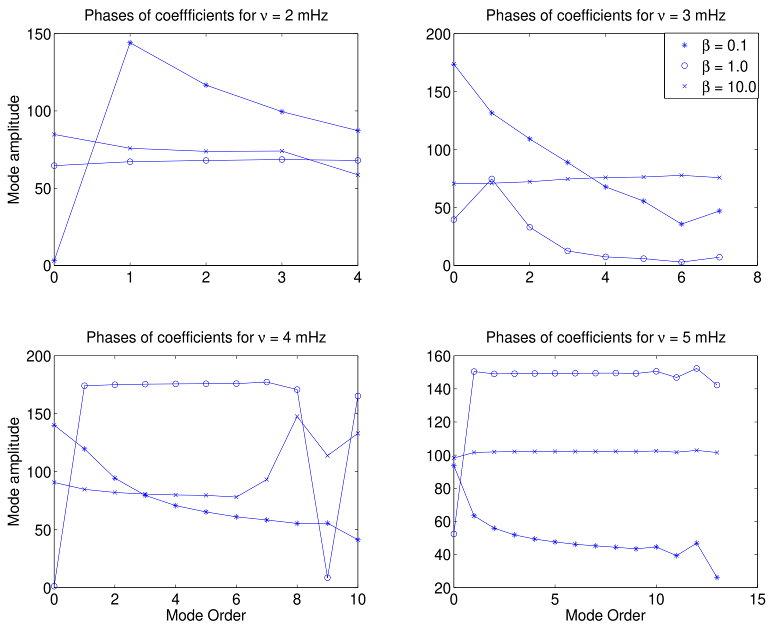

Figure 5.4 The phases of the scattered resonant modes a function of mode number shown for various values of plasma-β and frequency, ν. The legend applies to all panels.

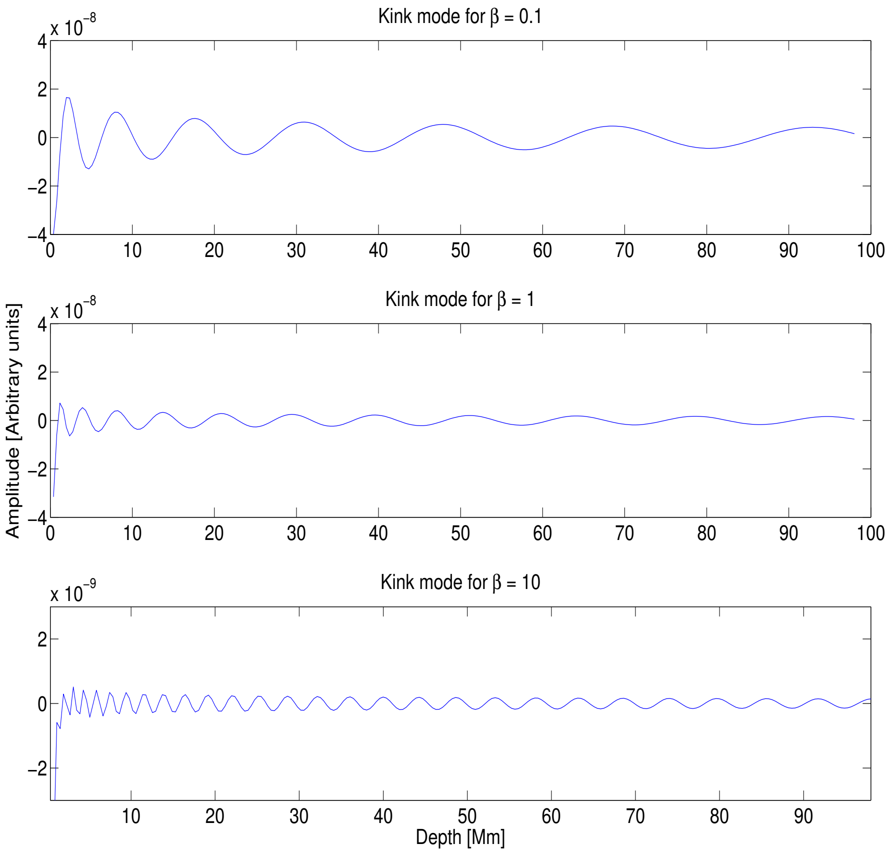

Figure 5.5 The kink mode for $\nu = 5$mHz. The magnetically dominated case with $\beta = 0.1$ is seen to be very stiff, as opposed to the $\beta = 10$ case.

Even under relatively idealized conditions as in this model, the manipulations required to recover the scattering properties are non-trivial.

Assuming that the scattering magnitude goes linearly with the number of these model flux tubes, our calculations seem to indicate that two flux tubes are perhaps sufficient to mimic the extent of the scatter. However, it must be said that the phases of the f mode coefficient differs significantly from data. We do not have an explanation for the poor phase agreement. Perhaps full blown numerical simulations are the only way to progress in this regard.

The various additional complexities apart, it is important to have a theoretical understanding and a model to appreciate the process of magneto-acoustic interactions. While numerical simulations are powerful tools to approach a more general set of problems, it is quite useful to develop an analytical treatment of a comparable situation, as we have attempted to do in this chapter. Such results can provide benchmarks to direct computations of these complex interactions.